



Surface subsidence caused by mantle plumes and volcanic loading in large igneous provinces

Wei Leng^{*}, Shijie Zhong

Department of Physics University of Colorado at Boulder, CO 80309, USA

ARTICLE INFO

Article history:

Received 9 November 2009
Received in revised form 30 December 2009
Accepted 8 January 2010
Available online 1 February 2010

Editor: Y. Ricard

Keywords:

large igneous province
surface uplifts
subsidence
mantle plume
loading

ABSTRACT

Large igneous provinces form with massive flood basalts being erupted over a large region within a few million years. A prevailing model for their formation is a mantle plume model in which a plume head originates from the core–mantle boundary, ascends through the mantle, and produces topographic uplift and eventually massive melting at the surface. However, many geological observations indicate surface subsidence in the central region before or during flood basalt eruptions. In this study, we demonstrate that a plume head temporarily ponding below the 660-km phase change boundary causes significant subsidence at the Earth's surface over an extended period before the eruption, and that the loading from erupted basalts causes surface subsidence at the periphery of the eruption area that affects the environment for subsequent episodes of basalt eruptions. Our studies therefore demonstrate that the observed subsidence history in many flood basalt provinces is characteristic of the dynamics of mantle plumes and may be used as diagnostics for identifying plume-induced flood basalt events.

© 2010 Elsevier B.V. All rights reserved.

1. Introduction

Large igneous provinces (LIP) form as a result of rapid eruptions of basaltic lavas over a large region and are widely observed at the Earth's surface (Coffin and Eldholm, 1994). The massive flood basalt eruptions have substantial effects on the Earth's climate and are generally believed to have caused mass extinctions in the Earth's history (Wignall, 2001; Wignall et al., 2009). A prevailing model for LIP formation is a mantle plume model in which a plume head originates from the Earth's deep interior, possibly the core–mantle boundary (CMB), ascends through the mantle, and when reaching the bottom of the lithosphere produces massive melting that is then followed by continuous but reduced level of melting associated with the plume tail (Richards et al., 1989; Campbell and Griffiths, 1990; Griffiths and Campbell, 1990).

Vertical motion history at the Earth's surface can be inferred from rock formations and stratigraphic sequences, and is one of the most important observations that pose constraints on tectonic processes (Czamanske et al., 1998; He et al., 2003; Saunders et al., 2007). Geodynamic studies of mantle plumes consistently predict surface uplifts of 1–2 km before and during the flood basalt eruptions (Griffiths and Campbell, 1991; Farnetani and Richards, 1994). This is consistent with geological observations of vertical motion history in some large igneous provinces (LIP) including the Emeishan and the North Atlantic Provinces that show transient surface uplifts of up to 1 km over several million years (Ma) immediately before the

eruptions (He et al., 2003; Saunders et al., 2007). The transient uplifts in the Emeishan LIP that was formed in the Late Permian were inferred from stratigraphic features of the Maokou Formation directly underlying the flood basalts (He et al., 2003).

Although the plume model is successful in explaining temporal and spatial patterns of volcanism and the surface uplifts associated with LIPs (Richards et al., 1991; Griffiths and Campbell, 1991; Farnetani and Richards, 1994; He et al., 2003; Saunders et al., 2007; Campbell, 2007), a significant difficulty with the plume model is to account for diverse geological observations of surface vertical motions, particularly subsidence, in some LIP regions before or during flood basalt eruptions (Richards et al., 1991; Czamanske et al., 1998; Hales et al., 2005; Peate and Bryan, 2008). Geological observations in these LIPs suggest significant surface subsidence over tens of millions of years before or during flood basalt eruptions that cannot be readily explained by the existing plume model.

Such surface subsidence was documented for the Siberian, Wrangellia, Columbia River and Emeishan LIPs. The Siberian Trap, the largest LIP on the continents, was formed at the end of Permian, and is underlain by the terrigenous sedimentary rocks of the Tungussskaya Series that were deposited between the Middle Carboniferous and the Late Permian. The deposition of the Tungussskaya Series was accompanied by significant surface subsidence based on paleogeographic and paleotectonic studies (Czamanske et al., 1998). Likewise, before the Wrangellia flood basalt eruption in the Early Triassic, the sedimentary rocks underlying the flood basalts reveal a variation of depositional environments from shallow-water in the Early Permian to deep-water in the Late Permian, indicating strong

^{*} Corresponding author. Tel.: +1 303 735 3048.
E-mail address: wei.leng@colorado.edu (W. Leng).

surface subsidence during the deposition (Richards et al., 1991). It has also been noted that for the Miocene Columbia River flood basalts the syn-eruption uplifts were preceded by moderate pre-eruption subsidence (Hales et al., 2005). For the Emeishan LIP, although the transient uplifts of several million years before the basalt eruptions were inferred (He et al., 2003), the deposition of the Maokou Formation and the underlying Qixia Formation is accompanied by regional-scale subsidence from the Early to Late Permian (Peate and Bryan, 2008 and references therein). The above geological observations indicate surface subsidence before flood basalt eruptions. On the other hand, recently, voluminous mafic hydromagmatic deposits and submarine extrusions were observed in the Emeishan LIP, suggesting a submarine environment at sea level for the flood basalt formation. The submarine environment for flood basalt formation indicates surface subsidence during flood basalt eruptions (Peate and Bryan, 2008). The observations of subsidence before and during flood basalt eruptions either motivated alternative, non-plume models for flood basalt formation (King and Anderson, 1995; Elkins Tanton and Hager, 2000), or were attributed to processes that are independent of mantle plumes and the flood basalt formation (Richards et al., 1991).

The goal of this study is to investigate surface vertical motion history in LIPs by considering more realistic physics in mantle dynamics and surface volcanic loading. We test two hypotheses. First, plume heads due to their high temperatures cause a reduced depth of the 660-km (ringwoodite to perovskite) phase change, and this leads to negative buoyancy that may offset the thermal buoyancy of mantle plumes and cause surface subsidence before basalt eruptions. Second, during the eruption process, the erupted basalts cause surface depression in the surrounding regions that affects the depositional environments for subsequent basalt eruptions. The 660-km phase change plays important roles in mantle dynamics on time scales of tens of millions of years, as suggested by seismically observed stagnant slabs in the mantle transition zones (Christensen and Yuen, 1985; Tackley et al., 1993; Fukao et al., 2009). The phase change may also significantly affect the dynamics of mantle plumes (Nakakuki et al., 1994; Davies, 1995). However, its effects on plume-induced surface dynamic topography were never examined.

2. Plume models

Our models of mantle plumes are in a cylindrically axisymmetric geometry and incorporate the 660-km phase change, compressibility, and depth- and strongly temperature-dependent viscosity. The non-dimensional conservation equations of mass, momentum and energy with anelastic liquid approximation are as below (Jarvis and McKenzie, 1980; Leng and Zhong, 2008b; King et al., 2009).

$$(\rho_r u_i)_i = 0, \quad (1)$$

$$-p_j \delta_{ij} + \tau_{ij} + \left[\rho_r \alpha g \text{Ra} (T - T_r) - \frac{\alpha g}{C_p \Gamma} p \chi - \text{Ra}_p \Psi_p \right] \delta_{i3} = 0, \quad (2)$$

$$\rho_r C_p \dot{T} + \rho_r C_p u_i T_{,i} + \rho_r \alpha g D_i u_3 (T + T_s) = (k T_{,i})_{,i} + \frac{D_i}{\text{Ra}} \tau_{ij} u_{i,j} + \rho_r H, \quad (3)$$

where ρ_r , u , p , τ , α , g , T , T_r , C_p , Γ , Ψ_p , T_s , k and H are radial density, velocity vector, dynamic pressure, deviatoric stress tensor, thermal expansivity, gravitational acceleration, temperature, reference temperature, specific heat at constant pressure, Grueneisen parameter, phase function for 660-km phase change, surface temperature, thermal conductivity and heat production rate, respectively; i and j are spatial indices and 3 means vertical direction; δ is the Kronecker delta function. \dot{T} is the derivative of temperature with respect to time t . The Rayleigh number Ra , phase change Rayleigh number Ra_p , dissipation number D_i and mantle compressibility χ are defined as

$$\text{Ra} = \frac{\rho_0 \alpha_0 g_0 \Delta T d^3}{\kappa_0 \eta_0}, \quad (4)$$

$$\text{Ra}_p = \frac{\Delta \rho_p g_0 d^3}{\kappa_0 \eta_0}, \quad (5)$$

$$D_i = \frac{\alpha_0 g_0 d}{C_{p,0}}, \quad (6)$$

$$\chi = \frac{D_i}{\Gamma_0}, \quad (7)$$

where ρ_0 , α_0 , g_0 , ΔT , d , κ_0 , η_0 , $\Delta \rho_p$, $C_{p,0}$ and Γ_0 are dimensional numbers of surface density, surface thermal expansivity, surface gravitational acceleration, temperature contrast between surface and the CMB, mantle thickness, surface thermal diffusivity, reference viscosity, density increase at 660-km phase change, surface specific heat at constant pressure and surface Grueneisen parameter, respectively (see Table 1). Eqs. (1)–(3) are non-dimensionalized with the following scalings: $x_i = x'_i/d$, $t = t'k_0/d^2$, $T = (T' - T'_s)/\Delta T$, $p = p'd^2/(\eta_0 \kappa_0)$, $H = d^2 H_0/(\kappa_0 \Delta T C_{p,0})$, where x_i and t are length in direction i and time, respectively. Symbols with primes are corresponding dimensional values. Details of the derivations of these equations can be found in Leng and Zhong (2008b).

The gravitational acceleration g and specific heat C_p are assumed to be constant. And the thermal expansivity α and thermal diffusivity $\kappa = k/(\rho_0 C_{p,0})$ are depth-dependent in our models (see Table 1). We employ the Adams–Williamson equation (Birch, 1952) as the equation of state, so the radial density profile ρ_r is given as (Leng and Zhong, 2008b)

$$\rho_r(z) = \exp[z\chi], \quad (8)$$

where z is the non-dimensional depth. The non-dimensional heat production rate H is fixed at 20.0 in our models and simple testing runs show that our results are insensitive to variations of this parameter.

We use a modified version of the 2-D Citcom code (Moresi et al., 1996) that considers axisymmetric geometry (Zhong and Hager, 2003) and mantle compressibility (Leng and Zhong, 2008b; King et al., 2009). In particular, we introduce a self-adaptive coordinate transformation integration scheme that significantly improves the accuracy of our axisymmetric models (Appendix A). We use 257 by 257 grids in a one by one box with mesh refinements in the top and bottom thermal boundary layers (TBL), near the phase boundary and near the centerline. The boundary conditions are isothermal and free-slip for the top and bottom boundaries and insulating and free-slip boundaries for the sidewalls. For simplicity, we only include the 660-km phase change and ignore the effects of latent heat. The initial thickness of the top and bottom TBLs are both 100 km. The initial

Table 1
Physical parameters and constants.

Parameters	Value
Mantle thickness d	2870 km
Surface thermal expansivity α_0^a	$4 \times 10^{-5}/\text{K}$
Surface thermal diffusivity κ_0^a	$7 \times 10^{-7} \text{ m}^2/\text{s}$
Surface density ρ_0	3400 kg/m ³
Surface specific heat $C_{p,0}$	1000 J/(kgK)
Surface gravitational acceleration g_0	10.0 m/s ²
Mantle compressibility χ	0.5
Dissipation number D_i	1.2
Surface temperature $T_{s,0}$	273 K
Temperature contrast between surface and bottom ΔT	3500 K
Internal heat production rate H_0	$5.9 \times 10^{-12} \text{ W/kg}$
Density increase for the phase change $\Delta \rho_p$	388 kg/m ³
Water density ρ_w	1000 kg/m ³
Density of basalts ρ_c	2800 kg/m ³
Elastic thickness of the lithosphere T_e	50 km
Young's modulus E	70 GPa
Poisson's ratio ν	0.25

^a Thermal expansivity decreases by a factor of 5 from surface to the CMB, while thermal diffusivity increases by a factor of 2.18 from surface to the CMB.

temperature profiles for our models are set as following. We consider the mantle interior temperature as $T_{adi}(z)$ which follows the adiabatic gradient. From Turcotte and Schubert (2002, page 187) we have,

$$\frac{dT_{adi}}{dz} = \frac{\alpha g T_{adi}}{C_p} \quad (9)$$

The non-dimensional form of Eq. (9) is (Leng and Zhong, 2008a)

$$\frac{dT_{adi}}{dz} = \alpha D_i (T_{adi} + T_s) \quad (10)$$

Given that the mantle average temperature at 100 km depth is ~ 1280 °C (Turcotte and Schubert, 2002) or 0.366 in non-dimensional

form, $T_{adi}(z)$ can be obtained from integration of Eq. (10). In the top TBL, the initial mantle temperature linearly decreases from $T_{adi}(z)$ at 100 km depth to the surface temperature, 0.0; and in the bottom TBL, the initial mantle temperature linearly increases from $T_{adi}(z)$ at 100 km above the CMB to 1.0, the non-dimensional CMB temperature. An initial perturbation in temperature is introduced in a small volume with a radius of 100 km in the bottom TBL near the centerline in which temperature is set to be equal to the bottom temperature to initiate the plume at the center of the cylinder. The Rayleigh number Ra is 2.0×10^7 , corresponding to a reference viscosity η_0 as 8.0×10^{21} Pa s. A temperature- and depth-dependent rheology in non-dimensional form is employed as:

$$\eta(T, z) = \eta_r(z) \exp[-A(T - T_{adi}(z))], \quad (11)$$

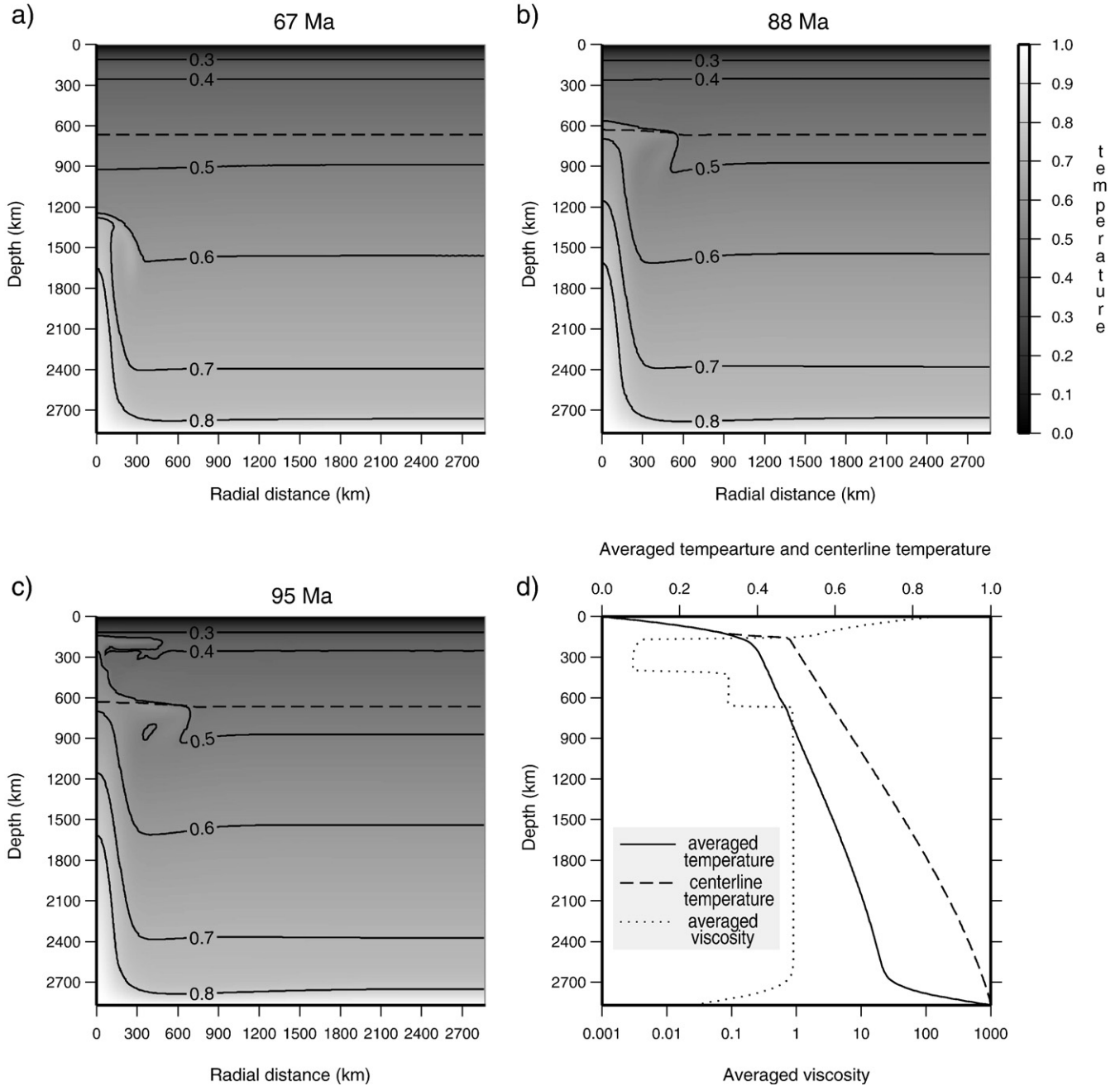


Fig. 1. Snapshots of non-dimensional temperature field at different time frames for case A01 (a)–(c), and horizontally averaged temperature and viscosity structure at different depths (d). a) For the plume head in the lower mantle; b) for the plume ponding below the phase change boundary; c) for the plume spreading out beneath the bottom of the lithosphere. Dashed lines in the temperature fields indicate the 660-km phase boundary. d) The horizontally averaged mantle temperature and viscosity, and centerline temperature, for temperature field shown in c).

where η is the non-dimensional viscosity. $\eta_r(z)$ is 1/300 and 1/10 in the asthenosphere (150 km < depth < 410 km) and the transition zone (410 km < depth < 660 km), respectively, and is otherwise 1.0. A non-dimensional activation energy $A = 13.8155$ is chosen, which leads to a strong temperature-induced viscosity contrast of $\sim 10^6$. Note that we use a linearized temperature-dependent viscosity (i.e., Eq. (11)), which is a good approximation of Arrhenius rheology except for low temperature. We will discuss the effects of depth-dependent viscosity profiles and activation energy in the next section.

Compared with previous plume models (e.g. Farnetani and Richards, 1994; Nakakuki et al., 1994; Davies, 1995), two key improvements in our models are the compressibility and strongly temperature-dependent viscosity (6 orders of magnitude of viscosity variations due to temperature effects). However, our models ignore a possible chemically dense layer above the CMB (Farnetani, 1997; Lin and van Keken, 2005). Mantle compressibility has significant effects on mantle plume temperatures (Leng and Zhong, 2008a). Similar to previous studies (e.g. Nakakuki et al., 1994; Davies, 1995), a plume is initiated at the CMB by perturbing CMB temperatures, and our models quantify the subsequent plume growth and ascent in the mantle and the resulting surface dynamic topography.

3. Results from plume models

Fig. 1 shows snapshots of temperature fields at three different times for case A01 with a Clapeyron slope $\gamma = -3.0$ MPa/K. After a plume forms from the CMB, the plume head rises through the lower mantle and reaches the 660-km phase boundary at ~ 74 Ma (Fig. 1a and b). The plume head, due to its high temperature, deflects the phase boundary upward, thus producing negative buoyancy that causes plume materials to pond, accumulate and spread below the phase boundary (Fig. 1b). After ~ 14 Ma or at ~ 88 Ma, the plume materials flush through the phase boundary into the upper mantle and reach the bottom of the lithosphere at ~ 92 Ma, and then spread below the lithosphere to a radius of 500–600 km within 2–3 Ma (Fig. 1c). This process is similar to that in previous studies (Farnetani and Richards, 1994; Nakakuki et al., 1994; Davies, 1995). The plume excess temperature is controlled by the mantle dissipation number and decreases as the plume ascends from the CMB to the upper mantle (Leng and Zhong, 2008a) (Fig. 1d). At ~ 300 km depth, the non-dimensional plume excess temperature is ~ 0.1 (i.e. ~ 350 K), consistent with surface observations (Schilling, 1991). Since the model calculations only last for ~ 100 Ma, the mantle temperature does not evolve much during the whole process and the average temperature shown in Fig. 1d is quite similar to the initial temperature profile.

Fig. 2a shows the surface dynamic topography for the three time frames shown in Fig. 1. When the plume head ascends in the lower mantle, it produces small surface dynamic uplift (Figs. 1a and 2a). However, when the plume ponds below the phase boundary, the negative buoyancy from the deflected phase boundary offsets the plume's thermal buoyancy and causes flow pattern in the upper mantle to reverse from upwelling to downwelling. Although the downwelling flow in the upper mantle is quite small in magnitude compared to the plume velocity in the lower mantle, the reversed flow produces significant (> 100 m) surface dynamic subsidence in the central region (Figs. 1b and 2a). After the plume materials flush through the phase boundary, the surface rapidly uplifts to ~ 1 km. Fig. 2b shows the time dependence of averaged surface dynamic topography in the central region (i.e. within 50 km in radius). For $\gamma = -3.0$ MPa/K, the subsidence lasts for ~ 14 Ma and reaches to ~ 100 m as the plume materials spread beneath the phase boundary. Notice that the dynamic topography are computed as $\delta h = \sigma_{zz} / \Delta \rho g$, where σ_{zz} is the surface normal stress and $\Delta \rho$ is the density contrast between the mantle and surface covering materials. The ~ 100 m dynamic subsidence is computed with water covering the surface and $\Delta \rho = 2400$ kg/m³. If the surface is covered by sediments, the density con-

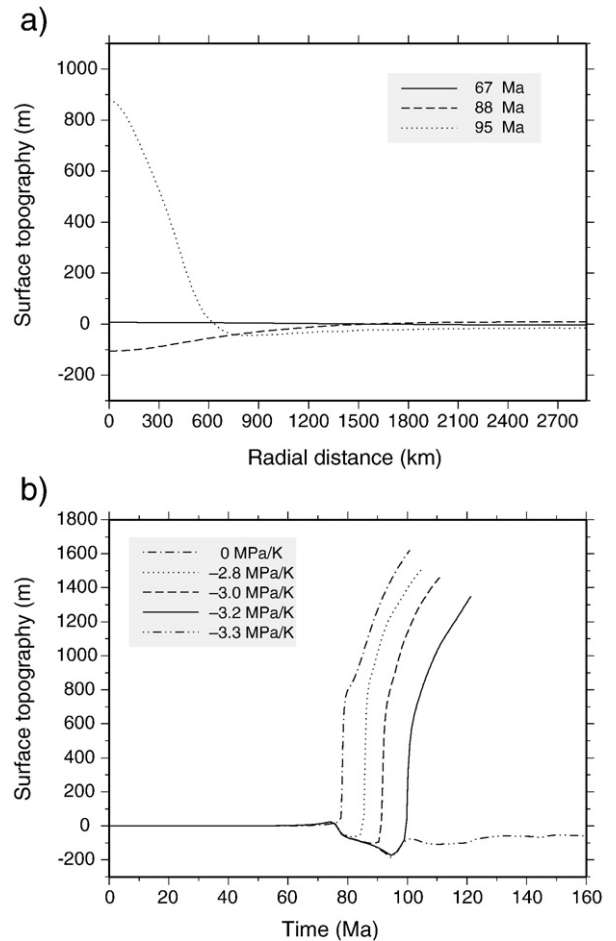


Fig. 2. (a) Surface dynamic topography profiles at three different times corresponding to the three temperature fields shown in Fig. 1a–1c. (b) The horizontally averaged dynamic topography within 50 km distance from the center above the plume versus time for cases with different Clapeyron slopes. The dynamic topography are computed as $\delta h = \sigma_{zz} / \Delta \rho g$, where σ_{zz} is the surface normal stress. For positive δh in subaerial environments, we use $\Delta \rho = \rho_0$, while for negative δh , we use $\Delta \rho = \rho_0 - \rho_w$, considering that the surface is covered by water.

trast between sediments and the mantle can be as small as 600 kg/m³, and ~ 100 m of dynamic subsidence implies possible accumulation of ~ 400 m thick sediments. Our model, therefore, suggests that significant uplifts above the plume only start to occur ~ 4 Ma before basalt eruptions as the plume reaches to and spreads below the lithosphere, and more importantly the uplifts are preceded by long periods (> 10 Ma) of subsidence, consistent with geological observations (He et al., 2003; Saunders et al., 2007; Richards et al., 1991; Czamanske et al., 1998; Hales et al., 2005; Peate and Bryan, 2008).

The Clapeyron slope, γ , is a crucial parameter for this process. From mineral physics and seismic studies, γ is around -3.0 MPa/K (Fukao et al., 2009). We computed additional cases in which γ is varied from 0 to -3.3 MPa/K, while keeping other parameters fixed as in case A01. The smaller $|\gamma|$, the smaller the surface subsidence is and the shorter time the subsidence lasts (Fig. 2b). Fig. 3 shows the maximum amplitude and the total time duration of the subsidence for different Clapeyron slopes. For $\gamma = -3.2$ MPa/K, the subsidence is ~ 200 m and lasts for ~ 20 Ma. While for $\gamma = -3.3$ MPa/K, the plume head is completely stopped and cannot ascend to the upper mantle (Fig. 2b). We define the amount of ponded plume buoyancy B immediately before the plume materials flush into the upper mantle as

$$B = \int \rho \alpha (T - T_{ave}(z)) dV, \quad (12)$$

where ρ , and $T_{ave}(z)$ are density and horizontally averaged temperature at depth z , respectively, and the integration is from the phase

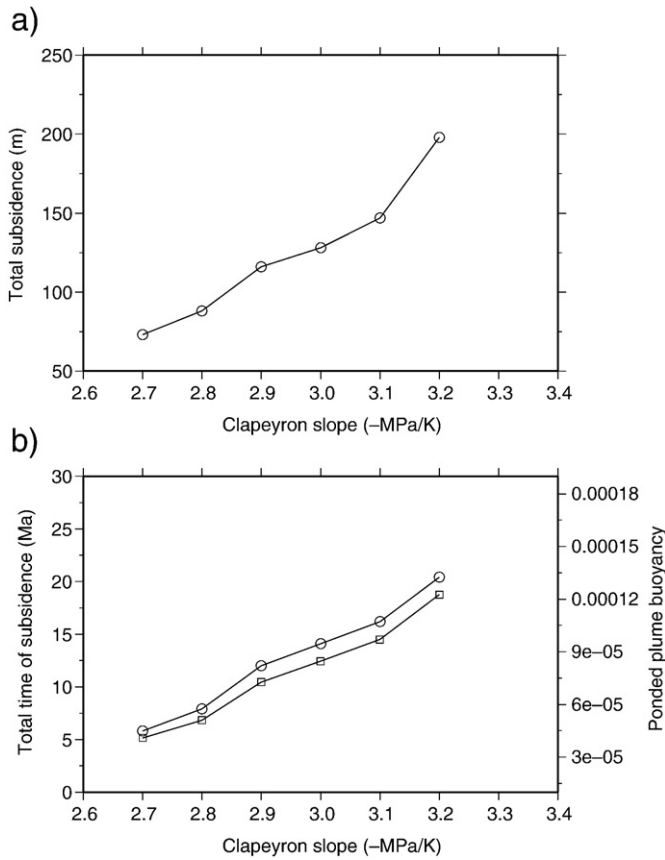


Fig. 3. The maximum amplitude (a) and the total time duration (b) of the subsidence versus the Clapeyron slopes (in circles). In (b), the amount of ponded plume buoyancy B immediately before penetration is also plotted (in squares) for different cases.

boundary to the 860 km depth. The ponded plume buoyancy below the phase boundary shows nearly the same dependence on γ as the duration and magnitude of the subsidence (Fig. 3b), suggesting that the subsidence is largely controlled by the ponded plume buoyancy, i.e. by the supply of the new hot materials from the bottom thermal boundary layer during ponding.

Fig. 4 shows the time dependence of averaged surface dynamic topography in the center region for different depth-dependent viscosity profile and different activation energy. Our results are relatively insensitive to the depth-dependent viscosity profiles (Fig. 4a), but are sensitive to the activation energy when it is small. For small activation energy which is generally used in previous plume studies (Farnetani and Richards, 1994; Nakakuki et al., 1994; Davies, 1995), a plume head readily penetrates through the phase boundary with insignificant surface subsidence (Fig. 4b). However, once the activation energy is sufficiently large (>5 orders of magnitude viscosity variations), our results become insensitive to this parameter (Fig. 4b).

4. Loading models and results

We now test the second hypothesis on the effects of volcanic loading on surface vertical motions that although evident in many volcanic constructs (e.g., Hawaii), are rarely discussed in studies of LIPs. Here, using a thin elastic plate model with 50-km elastic thickness, we compute the surface deflection caused by axisymmetric loads of erupted basalts (Brotchie and Silvester, 1969) and then determine the combined topography by superimposing the load-induced deflection onto a characteristic plume-induced topography. In our loading model in a cylindrically axisymmetric geometry, the cross-sectional shape of the basalt loads is maintained as a trapezoid, as shown in Fig. 5a, which represents a truncated cone or frustum. The

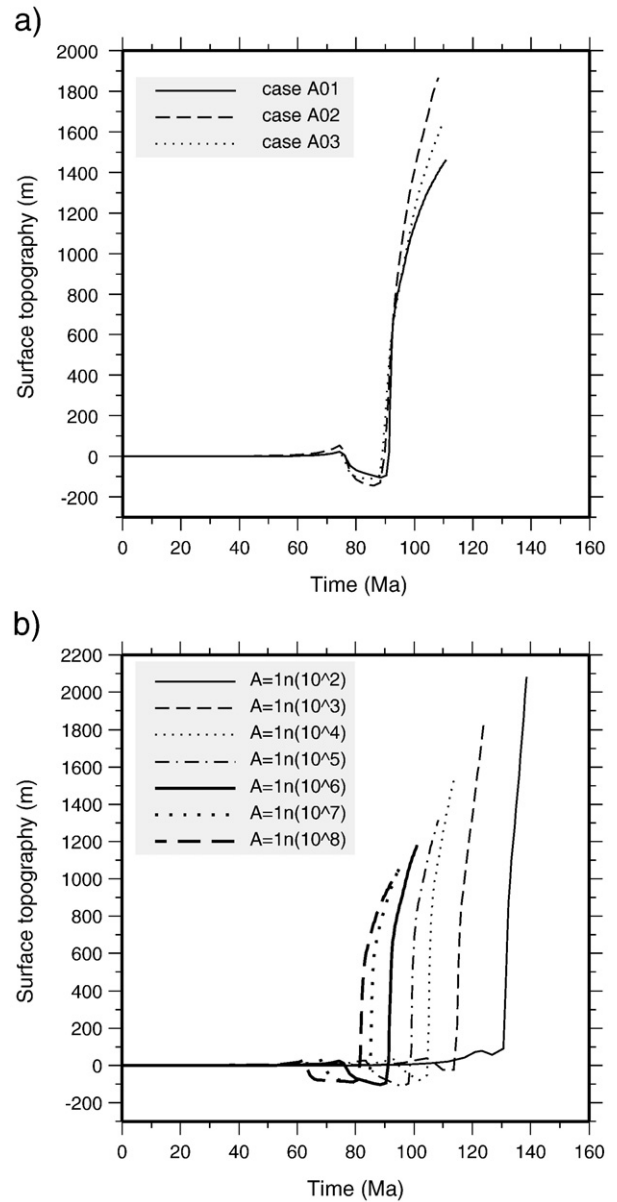


Fig. 4. (a) The dynamic topography in the center region above the plume versus time for cases with different depth-dependent viscosity structures. The solid line shows the results from the standard case A01. The dashed line shows the results from a case A02 which is the same as case A01 except that the $\eta_p(z)$ in the upper mantle ($150 \text{ km} < \text{depth} < 660 \text{ km}$) is uniformly $1/30$; The dotted line shows the results from a case A03 which is the same as case A01 except that the $\eta_p(z)$ in the upper mantle ($150 \text{ km} < \text{depth} < 660 \text{ km}$) is uniformly $1/50$. It can be observed that the variations of viscosity structure do not significantly affect the subsidence pattern. (b) The dynamic topography in the center region above the plume versus time for cases with different activation energy A . These cases are similar to the case A01, differing primarily in that they have different activation energy which leads to different temperature-dependent viscosity contrasts of $\sim 10^2$ to $\sim 10^8$. Notice that with small activation energy, the subsidence caused by the phase change is quite small. However, if the viscosity contrast is equal to 10^6 or larger, the subsidence patterns do not vary significantly.

bottom radius of the basalts increases at a steady rate of 300 km/Ma. The top radius of the loads is always 10% smaller than the bottom radius. The height of the basalt loads is set to be constant (e.g., 2 km).

The plume-induced topography is taken from case A01 at 95 Ma after the plume spreads below the lithosphere as shown in Fig. 2a and is assumed to be fixed with time, which is justified considering that the plume-induced uplifts mainly occur before basalt eruptions (He et al., 2003). We employ a simple loading history in which 2-km thick basalt loads grow at a steady rate of 300 km/Ma in the radial direction. When the basalt loads expand to 300 km in radius (i.e., after 1 Ma growth),

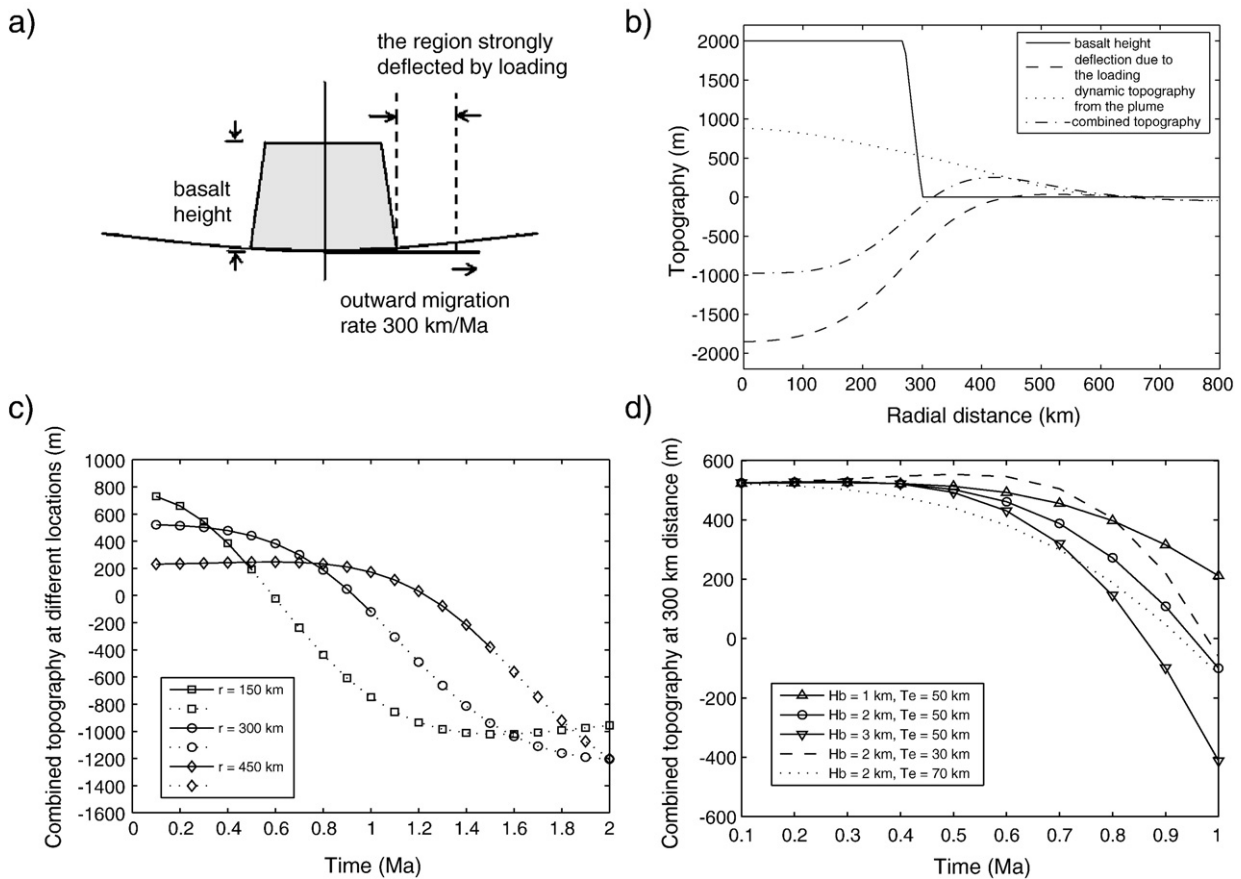


Fig. 5. (a) A schematic drawing for the loading of erupted basalts and its effects on the deflection of the surface (not to scale). (b) The deflection caused by the loading of the basalts on a 50 km thick elastic plate, the dynamic topography induced by the plume at 95 Ma for case A01, and the combined topography. (c) The combined topography at three locations ($r = 150$ km, 300 km, and 450 km) versus time as the basalt loads grow in radius from 0 to 600 km over 2 Ma. The solid lines show the combined topography before the surface is covered by basalts at the corresponding locations, while the dashed lines are the combined topography after the surface is covered by basalts. (d) The combined topography at $r = 300$ km versus time before this location is covered by basalts. Different curves show the effects of the basalt thickness, H_b , and the elastic thickness, T_e , on the combined surface topography.

they cause significant surface depression in the surrounding regions that is large enough to offset the plume-induced uplifts there (Fig. 5b). Fig. 5b shows the dynamic topography from the plume and the deflection due to the loading. It can be observed that at ~ 300 km in radial direction, the combined topography from these two components is negative. As a result, subsequent basalt eruptions in the surrounding regions are expected to occur near sea level, if these regions are near sea level before the plume-induced uplift happens. This mechanism may reconcile the observations of the mafic hydromagmatic deposits and submarine basalt eruptions in some areas of the Emeishan LIP (Peate and Bryan, 2008) with plume models. Fig. 5c shows the combined topography versus time at different locations in radial direction. With the linear growth history of basalts, the syn-eruption vertical motion is dominated by subsidence for most of the regions (e.g. $r = 300$ km and $r = 450$ km in Fig. 5c). However, in the central region (e.g. $r = 150$ km in Fig. 5c) where the plume-induced topography is large, the load-induced subsidence is insufficient to offset the plume-induced topography before the region is covered by basalts. We tested the effects of different basalt thickness and different elastic thickness of the plate on our results at $r = 300$ km. The load-induced subsidence is larger for thicker basalts, but is not sensitive to elastic thickness in the range of 30 km to 70 km (Fig. 5d).

5. Discussions and conclusions

We only account for the ringwoodite to perovskite phase change at 660-km depth and we use the density jump in the density profile from the Preliminary Reference Earth Model (Dziewonski and Anderson, 1981) as the density increase for the phase change, $\Delta\rho_p$ (Table 1).

However, only 60%–70% mantle materials undergo this phase change at 660-km depth, while other components in the transition zone may have different Clapeyron slopes at slightly different depths, e.g. the phase change of garnet to perovskite at ~ 700 km depth has positive Clapeyron slope (Fukao et al., 2009). Therefore, our results may overestimate the effect of ringwoodite to perovskite phase change which may require further studies. There are also other phase changes in the Earth's mantle. The 410-km phase change (i.e. olivine to wadsleyite) enhances the mantle flow at the phase boundary (e.g., Schubert et al., 1975), but should not affect our results on the plume ponding below the 660-km phase change. After the plume penetrates through the 660-km phase boundary, the 410-km phase change may increase the ascending velocity of the plume and shorten the time span between the plume penetration and the flood basalt eruptions. The newly discovered perovskite to post-perovskite phase change at the bottom of the mantle (Murakami et al., 2004; Oganov and Ono, 2004) only occurs for cold regions such as beneath subduction zones, and should not affect the dynamics of plumes that we consider here. We ignored the latent heating effect for phase changes and for melting process. The latent heating from 410-km and 660-km phase changes cancels each other and only slightly raises the mantle temperature in the transition zone (e.g., Schubert et al., 1975), thus should have little effects on our results. However, when the plume reaches the bottom of the lithosphere and the melting process occurs, latent heating effect during melting may significantly reduce the plume temperature as well as the surface dynamic topography. As a result, future studies should incorporate a realistic melting process and investigate its effects on plume-induced surface dynamic topography.

Subduction processes may significantly affect mass exchange across the 660-km phase boundary (Christensen and Yuen, 1985;

Tackley et al., 1993; Zhong and Gurnis, 1994). Although our plume models, like previous plume studies (e.g. Farnetani and Richards, 1994; Nakakuki et al., 1994; Davies, 1995), did not include subduction, we think that our phase change mechanism for pre-eruption surface subsidence above a plume is robust. However, we suggest that the slabs may modulate plume penetration through the phase boundary, leading to variable trapped plume buoyancy and ponding times. This may explain the observed variability in the durations and amplitude of pre-eruption subsidence (Richards et al., 1991; Czamanske et al., 1998; Hales et al., 2005; Peate and Bryan, 2008) and also the different sizes of LIPs (Ernst and Buchan, 2002).

In our loading models, we considered uniform basalt thickness in the range of 1 km to 3 km (Fig. 5d), which is consistent with the observed range of 1 km to 5 km (He et al., 2003; Saunders et al., 2007; Czamanske et al., 1998). Flood basalt eruptions are probably more sporadic and rapid (Wignall, 2001; Campbell, 2007) than assumed in our linear growth model. However, provided that episodes of basalt eruptions are separated by $> 10^5$ yr, which is the time scale for mantle stress relaxation below the elastic plate (Watts and Zhong, 2000), our results on load-induced depression in the vicinity of the erupted basalts remain valid.

In summary, our plume models for LIPs demonstrate that the rapid surface uplift, caused by plume buoyancy and lasting for ~ 4 Ma immediately before the flood basalt eruptions, is preceded by surface subsidence of tens of millions of years due to the effects of the 660-km phase change. During the basalt eruption, the erupted basalts may cause significant subsidence in surrounding regions, thus affecting the environment (submarine or subaerial) for subsequent flood basalts eruptions. These results reconcile the discrepancies between the observed surface motion history and the plume model in many LIPs. Particularly, the pre-eruption subsidence may provide new guidelines and diagnostics for identifying plume-induced flood basalt events.

Acknowledgements

We are grateful to Dr. Cinzia Farnetani who provides us with the benchmark notes for Stokes flow problem in cylindrically axisymmetric geometry. We thank Dr. Maxim Ballmer and an anonymous reviewer for constructive reviews that improved this manuscript. This study is supported by the National Science Foundation and David and Lucile Packard Foundation. The figures are plotted with GMT software < <http://gmt.soest.hawaii.edu/>>.

Appendix A. The self-adaptive coordinate transformation for integration in the axisymmetric finite element formulation

The original version of 2-D axisymmetric Citcom uses a standard Gauss quadrature in evaluating integrals at an element level. However, this may cause significant errors in normal stresses (i.e., dynamic topography) near the central line at $r=0$, as we shall see. The errors are caused by evaluating the singular numerical integration containing $1/r$ terms using the Gauss quadrature. The $1/r$ terms vary very quickly as $r \rightarrow 0$ and cannot be accurately calculated by the conventional Gauss quadrature. To solve this problem, we implement a self-adaptive coordinate transformation to evaluate the singular integration as $r \rightarrow 0$ (Telles, 1987; Clayton and Rencis, 2000).

We benchmarked our cylindrically axisymmetric code for isoviscous cases by comparing with the solutions from a propagator matrix method (Richards, 1986). With a density anomaly of a delta function at the middle depth of the mantle and a wave number of one, the surface horizontal velocity and normal stress can be analytically obtained from the propagator matrix method (Richards, 1986). With the Gauss quadrature, we found that the surface horizontal velocities from our code agree with analytical solutions within 0.1%. However, the results of surface normal stress show differences up to a few percent near the centerline where $r=0$ (Fig. A1). For a resolution of 65×65 grids, the difference is obvious for the two grid points closest to the centerline

(Fig. A1b). This kind of difference remains even with a very high resolution of 257×257 grids. However, the self-adaptive coordinate transformation improves the accuracy of the standard Gauss quadrature for singular integrals by shifting the Gaussian sampling points closer to the location of singularity (Telles, 1987; Clayton and Rencis, 2000). With this numerical treatment, the differences between the numerical results and the analytical results are reduced to be less than 0.1%, even with 65×65 grids (Fig. A1b). The details of the transformation can be found in Telles (1987). Notice that without the transformation method, the error of the normal stress close to $r=0$ can be much larger than a few percent for cases with complicated viscosity structures.

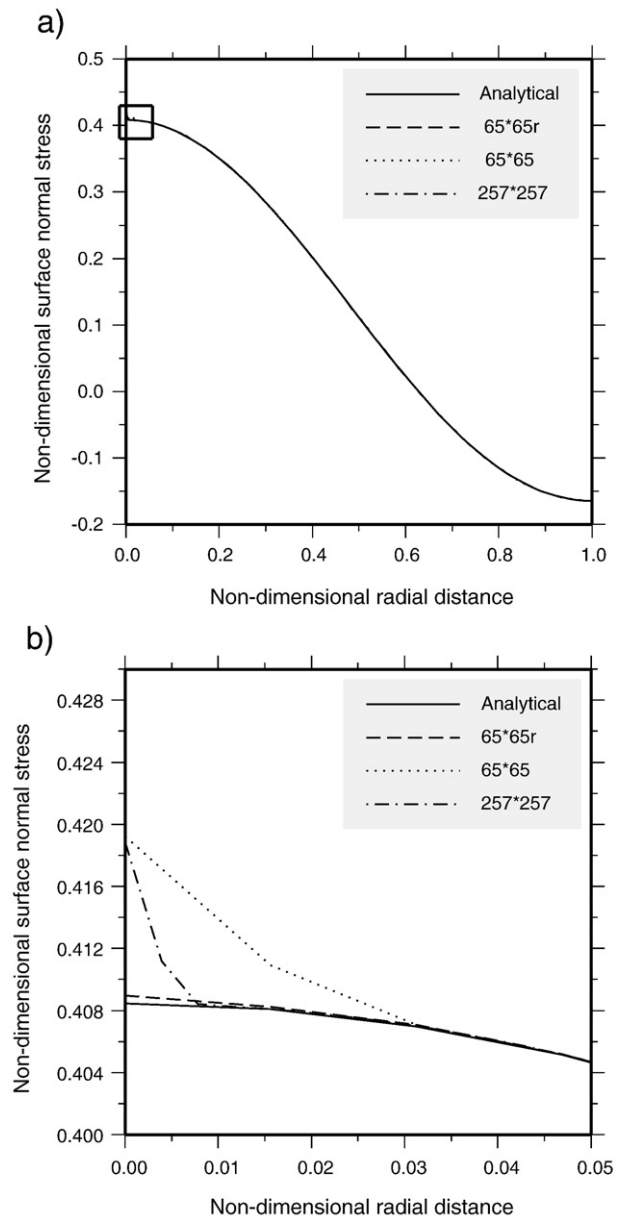


Fig. A1. (a) Benchmark results for non-dimensional surface normal stress. The central region is zoomed in and shown in (b). It can be observed that with the standard Gauss quadrature, the numerical results and analytical results agree quite well except at the two grid points close to $r=0$. However, with the self-adaptive coordinate transformation technique, as shown with “ 65×65 r”, the differences between the numerical results and the analytical results are reduced to be less than 0.1%.

References

- Birch, F., 1952. Elasticity and constitution of the Earth's interior. *J. Geophys. Res.* 57, 227–286.
- Brotchie, J.F., Silvester, R., 1969. On crustal flexure. *J. Geophys. Res.* 74, 5240–5245.
- Campbell, I.H., 2007. Testing the plume theory. *Chem. Geol.* 241, 153–176.
- Campbell, I.H., Griffiths, R.W., 1990. Implications of mantle plume structure for the evolution of flood basalts. *Earth Planet. Sci. Lett.* 99, 79–93.
- Christensen, U.R., Yuen, D.A., 1985. Layered convection induced by phase transitions. *J. Geophys. Res.* 90, 10,291–10,300.
- Clayton, J.D., Rencis, J.J., 2000. Numerical integration in the axisymmetric finite element formulation. *Adv. Eng. Softw.* 31, 137–141.
- Coffin, M.F., Eldholm, O., 1994. Large igneous provinces: crustal structure, dimensions, and external consequences. *Rev. Geophys.* 32 (1), 1–36.
- Czamanske, G.K., Gurevitch, A.B., Fedorenko, V., Simonov, O., 1998. Demise of the Siberian plume: paleogeographic and paleotectonic reconstruction from the prevolcanic and volcanic record, north-central Siberia. *Int. Geol. Rev.* 40, 95–115.
- Davies, G.F., 1995. Penetration of plates and plumes through the mantle transition zone. *Earth Planet. Sci. Lett.* 133, 507–516.
- Dziewonski, A.M., Anderson, D.L., 1981. Preliminary reference Earth model. *Phys. Earth Planet. Inter.* 25, 297–356.
- Elkins Tanton, L.T., Hager, B.H., 2000. Melt intrusion as a trigger for lithospheric foundering and the eruption of the Siberian flood basalts. *Geophys. Res. Lett.* 27 (23), 3937–3940.
- Ernst, R.E., Buchan, K.L., 2002. Maximum size and distribution in time and space of mantle plumes: evidence from large igneous provinces. *J. Geodynamics* 34, 309–342.
- Farnetani, C.G., 1997. Excess temperature of mantle plumes: the role of chemical stratification across D'. *Geophys. Res. Lett.* 24, 1583–1586.
- Farnetani, C.G., Richards, M.A., 1994. Numerical investigations of the mantle plume initiation model for flood basalt events. *J. Geophys. Res.* 99, 13,813–13,833.
- Fukao, Y., Obayashi, M., Nakakuki, T., the Deep slab project group, 2009. Stagnant slab: a review. *Annu. Rev. Earth Planet. Sci.* 37, 19–46.
- Griffiths, R.W., Campbell, I.H., 1990. Stirring and structure in mantle starting plumes. *Earth Planet. Sci. Lett.* 99, 66–78.
- Griffiths, R.W., Campbell, I.H., 1991. Interaction of mantle plume heads with the Earth's surface and onset small-scale convection. *J. Geophys. Res.* 96, 18,275–18,310.
- Hales, T.C., Abt, D.L., Humphreys, E.D., Roering, J.J., 2005. A lithospheric instability origin for Columbia River flood basalts and Willowa Mountains uplift in northeast Oregon. *Nature* 438, 842–845.
- He, B., Xu, Y., Chung, S., Xiao, L., Wang, Y., 2003. Sedimentary evidence for a rapid, kilometer-scale crustal doming prior to the eruption of the Emeishan flood basalts. *Earth Planet. Sci. Lett.* 213, 391–405.
- Jarvis, G.T., McKenzie, D.P., 1980. Convection in a compressible fluid with infinite Prandtl number. *J. Fluid Mech.* 96, 515–583.
- King, S.D., Anderson, D.L., 1995. An alternative mechanism of flood basalt formation. *Earth Planet. Sci. Lett.* 136, 269–279.
- King, S.D., Lee, C.Y., van Keken, P.E., Leng, W., Zhong, S.J., Tan, E., Tosi, N., Kameyama, M. C., 2009. A community benchmark for 2D Cartesian compressible convection in the Earth's mantle. *Geophys. J. Int.* 180, 73–87.
- Leng, W., Zhong, S.J., 2008a. Controls on plume heat flux and plume excess temperature. *J. Geophys. Res.* 113, B04408. doi:10.1029/2007JB005155.
- Leng, W., Zhong, S.J., 2008b. Viscous heating, adiabatic heating and energetic consistency in compressible mantle convection. *Geophys. J. Int.* 173, 693–702.
- Lin, S.-C., Van Keken, P., 2005. Multiple volcanic episodes of flood basalts caused by thermochemical plumes. *Nature* 436, 250–252.
- Moresi, L., Zhong, S.J., Gurnis, M., 1996. The accuracy of finite element solutions of Stokes' flow with strongly varying viscosity. *Phys. Earth Planet. Inter.* 97, 83–94.
- Murakami, M., Hirose, K., Kawamura, K., Sata, N., Ohishi, Y., 2004. Post-perovskite phase transition in MgSiO₃. *Science* 304, 855–858.
- Nakakuki, T., Sato, H., Fujimoto, H., 1994. Interaction of the upwelling plume with the phase and chemical boundary at the 670 km discontinuity: effects of temperature-dependent viscosity. *Earth Planet. Sci. Lett.* 121, 369–384.
- Oganov, A.R., Ono, S., 2004. Theoretical and experimental evidence for a post-perovskite phase of MgSiO₃ in Earth's D'' layer. *Nature* 430, 445–448.
- Peate, I.U., Bryan, S.E., 2008. Re-evaluating plume-induced uplift in the Emeishan large igneous province. *Nature Geosci.* 1, 625–629.
- Richards, M.A., 1986. Dynamical models for the Earth's geoid. Ph. D. thesis, Calif. Inst. Of Technol.
- Richards, M.A., Duncan, R.A., Courtillot, V.E., 1989. Flood basalts and hot-spot tracks: plume heads and tails. *Science* 246, 103–107.
- Richards, M.A., Jones, D.L., Duncan, R.A., Depaolo, D.J., 1991. A mantle plume initiation model for the Wrangellia flood basalt and other oceanic plateaus. *Science* 254, 263–267.
- Saunders, A.D., Jones, S.M., Morgan, L.A., Pierce, K.L., Widdowson, M., Xu, Y.G., 2007. Regional uplift associated with continental large igneous provinces: the roles of mantle plumes and the lithosphere. *Chem. Geol.* 282–318.
- Schilling, J.G., 1991. Fluxes and excess temperature of mantle plumes inferred from their interaction with migrating midocean ridges. *Nature* 352, 397–403.
- Schubert, G., Yuen, D.A., Turcotte, D.L., 1975. Role of phase transitions in a dynamic mantle. *Geophys. J. R. Astron. Soc.* 42, 705–735.
- Tackley, P.J., Stevenson, D.J., Glatzmaier, G.A., Schubert, G., 1993. Effects of an endothermic phase transition at 670 km depth in a spherical model of convection in the Earth's mantle. *Nature* 361, 699–704.
- Telles, J.C.F., 1987. A self-adaptive co-ordinate transformation for efficient numerical evaluation of general boundary element integrals. *Int. J. Numer. Methods Eng.* 24, 959–973.
- Turcotte, D.L., Schubert, G., 2002. *Geodynamics*, 2nd ed., Cambridge Univ. Press, New York.
- Watts, A.B., Zhong, S.J., 2000. Observations of flexure and the rheology of the oceanic lithosphere. *Geophys. J. Int.* 142, 855–875.
- Wignall, P.B., 2001. Large igneous provinces and mass extinctions. *Earth-Sci. Rev.* 53 (1), 1–33.
- Wignall, P.B., et al., 2009. Volcanism, mass extinction, and carbon isotope fluctuations in the middle Permian of China. *Science* 324, 1179–1182.
- Zhong, S.J., Gurnis, M., 1994. The role of plates and temperature-dependent viscosity in phase change dynamics. *J. Geophys. Res.* 99, 15,903–15,917.
- Zhong, S.J., Hager, B.H., 2003. Entrainment of a dense layer by thermal plumes. *Geophys. J. Int.* 154, 666–676.